ACS APPLIED MATERIALS & INTERFACES

Research Article

www.acsami.org

Direct-Write Deposition and Focused-Electron-Beam-Induced Purification of Gold Nanostructures

Domagoj Belić,[†,‡] Mostafa M. Shawrav,[†] Marco Gavagnin,[†] Michael Stöger-Pollach,[§] Heinz D. Wanzenboeck,*[,†] and Emmerich Bertagnolli[†]

[†]Institute of Solid State Electronics, Vienna University of Technology, Floragasse 7/1, A-1040 Vienna, Austria

[§]University Service Center for Transmission Electron Microscopy (USTEM), Vienna University of Technology, Wiedner Hauptstrasse 8−10/052, A-1040, Vienna, Austria

Supporting Information

ABSTRACT: Three-dimensional gold (Au) nanostructures offer promise in nanoplasmonics, biomedical applications, electrochemical sensing and as contacts for carbon-based electronics. Direct-write techniques such as focused-electron-beam-induced deposition (FEBID) can provide such precisely patterned nanostructures. Unfortunately, FEBID Au traditionally suffers from a high nonmetallic content and cannot meet the purity requirements for these applications. Here we report exceptionally pure pristine FEBID Au nanostructures comprising submicrometer−large monocrystalline Au sections. On the basis of high-resolution transmission electron microscopy results and Monte Carlo simulations of electron trajectories in the deposited nanostructures, we propose a curing mechanism that elucidates the observed phenomena. The in situ focused-electron-beam-induced curing mechanism was supported by postdeposition ex situ curing and, in combination with oxygen plasma cleaning, is utilized as a straightforward purification method for planar FEBID structures. This work paves the way for the application of FEBID Au nanostructures in a new generation of biosensors and plasmonic nanodevices.

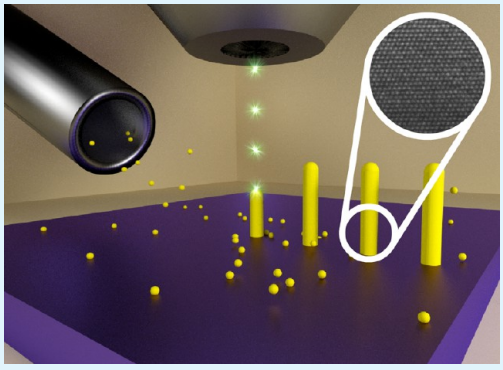

KEYWORDS: *FEBID, gold nanostructure, nanopillar, nanowire, purity, FEBIC, oxygen plasma cleaning*

INTRODUCTION

Top-down processes such as optical and electron-beam lithography are still the dominant nanostructuring methods but suffer from several restrictions because they are confined to planar substrates, rely on the use of photoresists, and require a number of subsequent steps to transform structures into the desired microarchitecture. To directly fabricate nanostructured materials on a whole range of substrates, an alternative, less rigid method is required. Recently, various resistless direct-write techniques have been introduced that allow for the direct deposition of more complex three-dimensional (3D) patterns on the nanoscale, in a single process step. Among these, direct-write deposition using an ion beam, called focused-ion-beam-induced deposition (FIBID), or using an electron beam, called focused-electron-beam-induced deposition (FEBID), has been implemented as a standard in novel dual-beam scanning electron/ion microscopy.[1−3] In both deposition techniques, volatile precursor molecules are introduced into the microscope chamber, usually through a nozzle, near the desired deposition spot on the substrate. When exposed to an electron or ion beam, the adsorbed precursor molecules decompose on the substrate surface, yielding a patterned deposit. In this way, by guiding the electron/ion beam precisely, one can deposit metallic nanostructures with a very high accuracy, down to a resolution of a single molecule.[4] Although FIBID is faster and more robust, it comes with major downsides: physical damage and contamination of the substrate caused by implantation of ions from the beam. The resulting deterioration of the structural and electronic properties of the underlying material is not acceptable for most applications. Here FEBID offers a solution because it is generally much gentler to the material (under the electron beam) and does not contaminate the substrate.

FEBID has already successfully proven its merits in a wide range of advanced nanoscale applications: apart from preparing contacts for nanoscale measurements,[5,6] it has also been used for patterning of stencil masks[7] and repairing of gate contacts,[8] the fabrication of field-emission tips,[9−11] immobilization and separation of nanoparticles,[12,13] template growth of nanowires (NWs),[14,15] and selective functionalization of customized nanostructures.[16] Recently, FEBID has been used in advanced nanodevices, e.g., to stabilize the polarization of vertical cavity surface-emitting lasers[17] or to fabricate ultrasmall Hall sensors[18] and nanomagnet logic devices.[19]

Received: October 22, 2014
Accepted: December 29, 2014
Published: December 29, 2014

DOI: 10.1021/am507327y
ACS Appl. Mater. Interfaces 2015, 7, 2467−2479

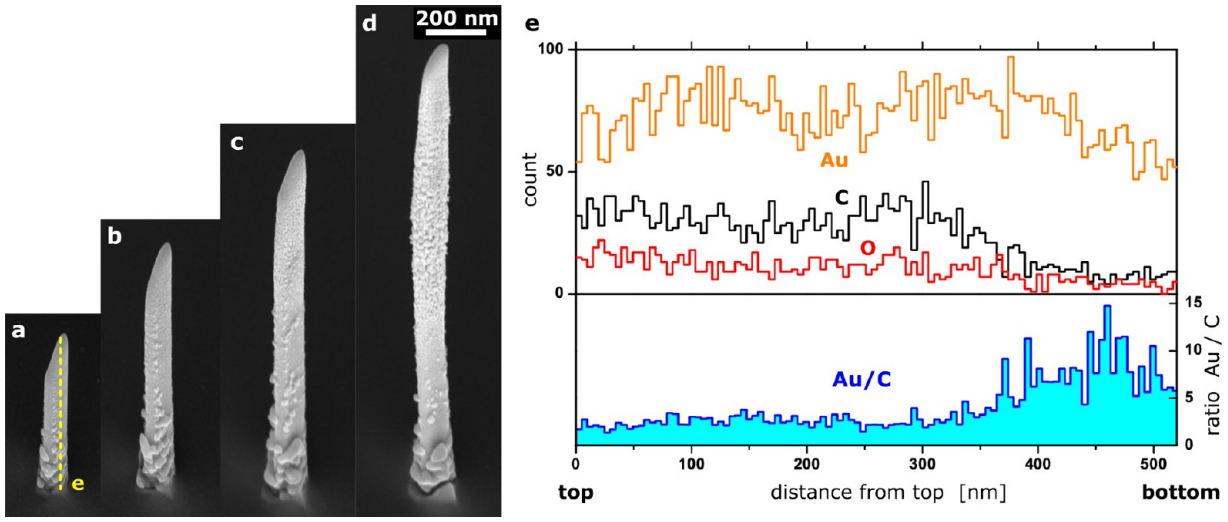

Figure 1. (a–d) SEM images of free-standing FEBID Au NPs deposited onto a Si substrate. The deposition time was 20 s (a), 40 s (b), 60 s (c), and 90 s (d). Note the presence of larger lumps in the bottom section of the NPs. (e) SEM–EDX results for the elemental composition of the NP in part a, as measured along the dashed line, showing a gradual increase of the Au content toward the base.

Among all FEBID materials, gold (Au) seems to be one of the most appealing substances because it possesses favorable chemical, electrical, and optical properties. Utilizing metal–organic precursors, FEBID Au has been used as a growth template for NWs[14,15] and as an electrode for metal–-oxide–semiconductor capacitors.[20] In particular, FEBID of Au nanostructures shows great potential for applications in plasmonics.[21−23] However, the main problem for wider usage of FEBID Au is significant carbon (C) contamination during deposition. Namely, when FEBID is performed in the vacuum environment of a microscope, a significant fraction of the metal–organic Au precursor molecules are only partially decomposed. In addition, decomposition of hydrocarbons from the residual gas in the scanning electron microscopy (SEM) chamber has a negative effect on the deposit purity. Consequently, FEBID Au nanostructures tend to suffer from C contamination, so a low Au content of less than ∼30 atom % is regularly achieved.[9,17,24] Recently, van Dorp and colleagues investigated a range of novel Au complexes as candidates for FEBID Au precursors, yielding pristine deposits with a Au fraction of up to ∼40 atom %.[25] So far, purification approaches occurring during FEBID, such as in situ substrate heating,[9,26] deposition in reactive environments,[27,28] or, very recently, laser-assisted FEBID,[29,30] have enhanced the metal content in deposits only moderately. Nevertheless, to achieve a major increase, additional laborious postdeposition purification steps are still required.[31,32] With a few exceptions, FEBID Au experiments made use of C-rich metal–organic precursors—dimethylgold(III) acetylacetonate (Me_2-Au-acac), dimethylgold(III) trifluoroacetylacetonate (Me_2-Au-tfa), or dimethylgold(III) hexafluoroacetylacetonate (Me_2-Au-hfa)—so a significant C fraction in the deposits was foreseeable. Only FEBID using the C-free precursor PF_3AuCl generated granular structures having a high Au content,[33,34] but its very unstable nature excludes wider technological usage. Generally, despite intense efforts, the low metallic content in FEBID Au materials is still the crucial problem.

In this work, we report on FEBID conditions that directly yield submicrometer grains of pure crystalline Au. We systematically address the issue of a relatively low Au fraction in vertical nanopillars (NPs) and planar areas produced by FEBID, using the common and stable metal–organic Au precursor Me_2-Au-tfa in a nonreactive environment. First, we show that by optimizing the deposition parameters—electron-beam current, accelerating voltage, and deposition time—it is possible to obtain free-standing FEBID NPs that contain sections of the highest Au content reported to date for any metal–organic Au precursor. Next, postdeposition electron-beam curing has been implemented on the FEBID Au material to elucidate the effect of electron irradiation on its structural and electrical properties. On the basis of the experimental findings, we propose a model of focused-electron-beam-induced curing (FEBIC) that explains the mechanism leading toward high-purity FEBID Au nanostructures. The FEBIC model was further supported by evidence only seen after postdeposition oxygen plasma treatment of the planar areas.

RESULTS AND DISCUSSION

The first set of fundamental experiments we performed will reveal whether variation of the deposition conditions—even for metal–organic precursors—can increase the purity of FEBID Au deposits above the standard threshold of 30 atom %. For this purpose, we deposited a range of free-standing Au NPs; by scanning the experimental parameter space spanned by the axes of the total deposition time, electron beam energy, and electron beam current (Figure S1 in the Supporting Information, SI) we could elucidate their effect on the growth rate and chemical composition of NPs. These selected parameters are generally applicable for all FEBID processes and have been identified as major impact factors on the Au deposition outcome.[20] In addition, they can be easily adapted on common FEBID systems. The full parameter space for deposition would also include further dimensions such as substrate type, precursor flux, substrate temperature, and beam scan parameters (dwell time and pixel spacing); however, because of experimental feasibility constraints, by choosing pillar geometry, we limited our investigation on the more universal FEBID parameters.

Overall, more than 500 samples were carefully deposited for the purpose of the study. Highly undesired proximity effects were avoided by keeping a large enough distance between the nanostructures.[12,35,36] Out of the total number of samples, more than 100 NPs were produced at identical parameters (HT

DOI: 10.1021/am507327y
ACS Appl. Mater. Interfaces 2015, 7, 2467−2479

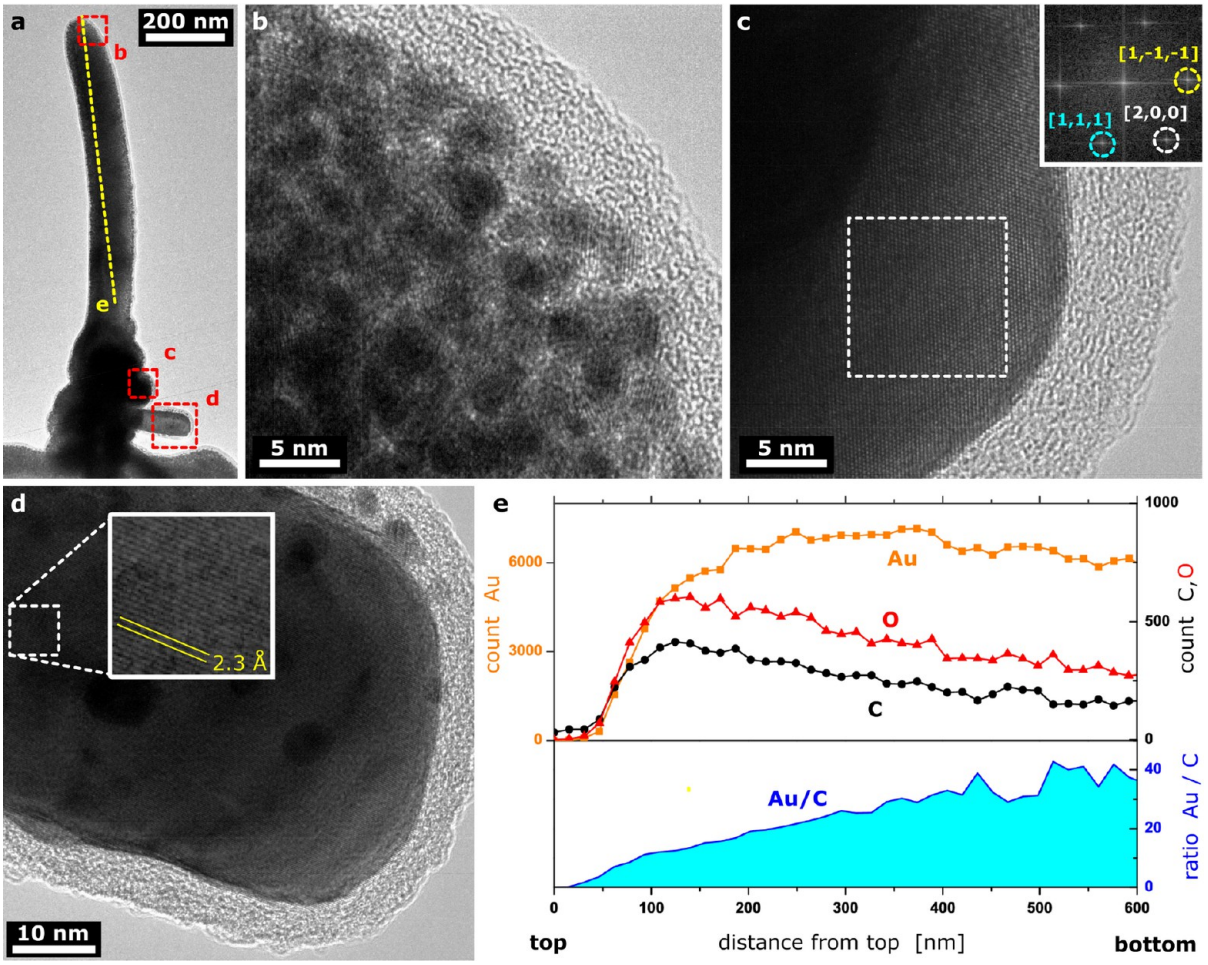

Figure 2. (a) BF-TEM image of a FEBID Au NP. Note the lumps (indicated as "c" and "d") visible at the base of the NP. (b) HRTEM image of the top section of the NP showing nanocrystals ranging in size from 3 to 6 nm embedded in an amorphous matrix. (c) HRTEM image of the lump in part a revealing that it is a single crystal sized in tens of nanometers. Inset: Fast Fourier transform of the indicated area revealing that the structure corresponds to the fcc Au lattice. (d) HRTEM image of the SNP from part a, demonstrating that it is an elongated single crystal covered with an amorphous shell. The close-up shows an interplanar distance of 2.3 Å, which matches the distance between {1, 1, 1} planes in the fcc Au lattice. (e) STEM−EDX linescan taken along the vertical axis of the NP, indicated by the dashed line in part a.

= 3 kV; I = 1 nA), and in this paper, only a representative selection can be shown, which is characteristic for the entire group. SEM analyses (Figure 1) suggest that, after a relatively short initial deposition (t < 20 s; I = 1 nA), FEBID Au NPs grow linearly in time, confirming previous observations.[37] Surprisingly, contrary to expectations based on a constant growth rate, the chemical composition of our Au NPs was not uniform. A meticulous SEM−energy-dispersive X-ray spectroscopy (EDX) analysis along the vertical (i.e., growth) axis of the NPs revealed a clear compositional gradient. For all investigated NPs, the Au fraction was significantly higher in the bottom (i.e., initially deposited) section of the NPs than in the top section (i.e., the section deposited last), with a gradual decrease of the Au content as one goes up the NP (Figure 1e). At the same time, the C content shows the opposite trend, with a high concentration of C at the top constantly decreasing toward the bottom. EDX results indicate that the Au content at the bottom of the NPs was as much as 3 times higher than that at the top (Figure S2 in the SI). This feature was common to all NPs exceeding 200 nm in height, for which reliable SEM−EDX linescans could be obtained. Because such consistent, substantial differences in the Au (and C) content between the base and top of the NPs surpass the intrinsic uncertainty of EDX, the gradient has to be a genuine compositional characteristic of our FEBID Au NPs. A detailed high-resolution (HR)SEM analysis revealed a clumped appearance of the NP surface, especially at the base region of the NPs, where a higher Au content was observed, with visibly larger lumps (>50 nm) present. Spot EDX measurements specifically performed on these lumps revealed an exceptionally high Au fraction (>70 atom %), which was significantly higher than that in any other part of the NPs. Having identified an unusually high Au content in our deposits from a standard metal−organic precursor, we proceeded toward untangling the mechanism leading to this trend.

In the second step, the genesis of such Au-rich nanostructures was deduced from transmission electron microscopy (TEM) studies. To gain detailed insight into the structure and composition of FEBID Au NPs, we prepared samples immediately suitable for TEM examination. In detail, we deposited a series of NPs onto the 0.2-mm-thick frame of a silicon (Si) window TEM grid, which was tilted 70° with respect to the electron beam, i.e., to the NP growth direction (Figure S3 in the SI). This procedure allowed for straightforward TEM investigation without further artifact-prone preparation steps (such as focused-ion-beam-induced

DOI: 10.1021/am507327y
ACS Appl. Mater. Interfaces 2015, 7, 2467−2479

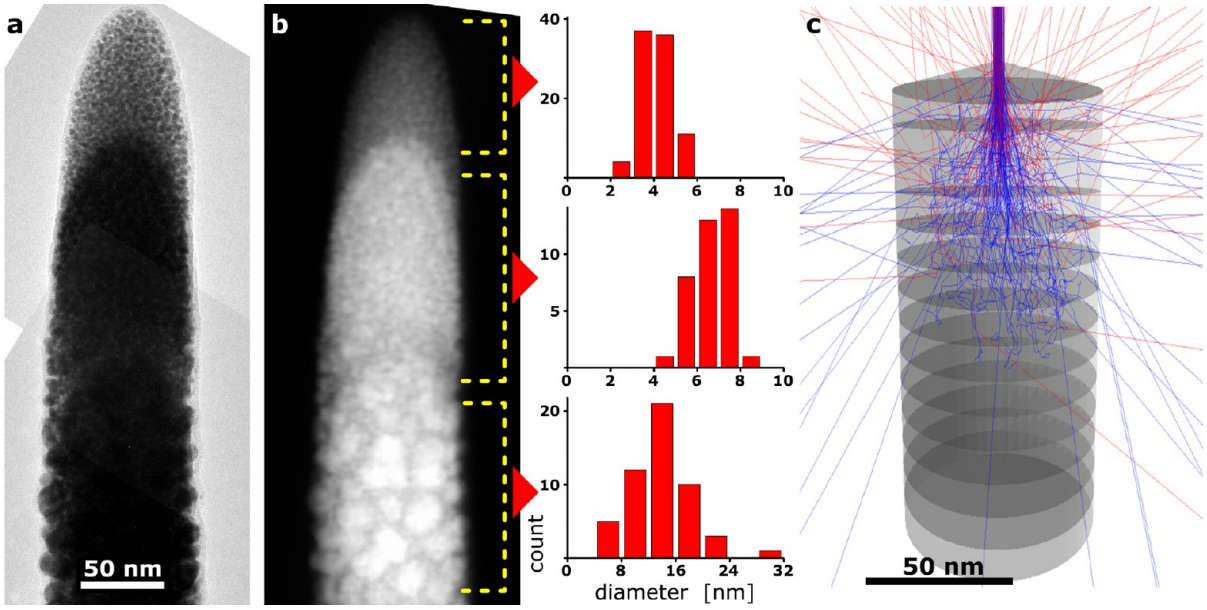

Figure 3. Montage of BF-TEM images (a) and the corresponding HAADF-STEM images (b) of the top and middle sections of a FEBID Au NP. The crystallite size increases from 4.1 ± 0.1 nm in the very top section to 6.7 ± 0.1 nm in the lower section to 13.9 ± 0.7 nm in the lowest section of the presented NP. Note the abrupt parabolic boundary ("curing front") approximately 70 nm from the top. (c) Results of Monte Carlo simulations of the penetration range and scattering of a 3 keV electron beam inside a NP consisting of cylindrical slices, with the Au content increasing from the top slice to the bottom by 1 atom % per slice. Backscattered electron trajectories are highlighted in red.

contamination). During deposition, a sufficient spacing distance of >2 μm between the individual NPs was maintained to avoid the proximity effects. In total, more than 50 Au NPs with a height of >500 nm were deposited onto the TEM grid using the sets of experimental parameters that had previously yielded free-standing NPs of the steepest Au gradient. It could be observed that the amount of deposited material was roughly constant for the given set of deposition parameters. For the same deposition time, the height of the NPs varied less than 10%, depending on the occurrence of lumps in the bottom NP sections: the more lumps, the shorter the NP's height. Bright-field (BF)-TEM of the Au NPs was combined with high-angle annular dark-field scanning TEM (HAADF-STEM) and scanning TEM (STEM)−EDX to simultaneously gather the complete information on both the structural and compositional profiles of the NPs. The BF-TEM investigation showed that without exemption all examined NPs had lumps at their base (Figure S4 in the SI), in line with the earlier SEM observation. Depending on the experimental parameters used for deposition of these NPs, the lumps varied in size and appearance from rather small (<30 nm) to relatively big, elongated structures (>100 nm). The general observation was that the latter were favored by a lower acceleration voltage, high beam current, and high precursor flux. Because of off-axis (i.e., sideway) extrusion from the main growth axis of the NP, these elongated lumps are referred to as side NPs (SNPs). In the most extreme case, a single whisker-type nanostructure having a number of SNPs was observed (Figure S4d in the SI). For the investigated parameter space as a rule, we observed that SNPs originate only from the bottom section of the NPs, up to a height of ~400 nm (measured from the substrate level). Interestingly, this value is very similar to the height that was previously identified as the border between two NP growth types.[37] Although this behavior indicates diffusive processes with a $t^{1/2}$ relationship, the effects of beam heating during the proceeding growth make it difficult to clearly conclude on the temperature-dependent effects of precursor diffusion and precursor desorption. However, experimental data points toward a shortage of precursor for a height above 400 nm.

The characteristics of SNPs are elucidated from a set of 18 reproducible HR(S)TEM observations representatively illustrated in Figure 2. This Au NP contains distinctive sections having a smoother pointed top (Figure 2a) and a rather lumpy base with several elongated SNPs. The close-up of the top (Figure 2b) reveals nanocrystals ranging in size from 2 to 6 nm embedded in an amorphous matrix. Their selected-area electron diffraction patterns correspond to the face-centered-cubic (fcc) lattice of bulk Au (Figure S5 in the SI). Such a form seems to be typical for pristine FEBID Au NPs produced in nonreactive environments.[5,10,26] However, contrary to previously reported NPs, we observe a novel extraordinary property of our FEBID Au NPs: the lumpy bottom sections contain single crystals of Au that are tens of nanometers across (Figure 2c). These Au crystals in the bottom sections are considerably bigger than the crystals present in the top section of the NPs. Moreover, the bottom section contains SNPs, which comprised an even larger single Au crystal covered with a relatively thin amorphous layer (Figure 2d). In the most extreme case, we observed an SNP exceeding 300 nm in length. Next, the Au content was investigated from the bottom section with the SNPs up to the SNP-free top of the vertical NP. Figure 2e presents a STEM−EDX linescan performed along the deposition axis of the NP: a gradual increase in the Au fraction from the top to the bottom of the NP is clearly evident and proves the high Au content in the bottom section, confirming our initial SEM−EDX results (Figure 1). Because of better vacuum conditions, STEM−EDX is deemed more reliable since it is less susceptible to C contamination, which is known to affect the quantification in SEM−EDX.[38] The STEM−EDX measurements revealed that the local area-averaged values of the Au fraction in the bottom sections were significantly higher than the area-averaged value obtained in the top section of the

DOI: 10.1021/am507327y
ACS Appl. Mater. Interfaces 2015, 7, 2467−2479

NPs (Figure S5 in the SI). The top section contains <30 atom % of Au (a value typical for FEBID Au structures so far), whereas the bottom section shows a local Au content of >70 atom %, with the peak value of ∼90 atom % acquired on the SNP presented in Figure 2d. HR(S)TEM and EDX investigations of all deposited NPs repeatedly showed very similar structural and compositional properties, indicating that SNPs are made of a single-crystal Au core covered with a relatively thin amorphous carbonaceous shell (<8 nm). These SNPs comprise the biggest FEBID Au single crystals reported so far, having *a width of up to 100 nm and a length of a few hundred nanometers*. To date, this is the first time that such high-purity pristine Au nanostructures have been produced by FEBID *from a stable metal−organic Au precursor in a nonreactive environment*. In light of the intensive efforts that have recently been invested in postdeposition purification of FEBID Au nanostructures,[26,31,32] such experimental realization of an exceptionally pure pristine FEBID Au material is highly anticipated.

In summary, the obtained results strongly indicate a reaction pathway that ultimately allows for direct writing of high-purity Au structures by standard FEBID using a metal−organic precursor. The following sections are therefore dedicated to unveiling the reaction mechanisms. In our interpretation, we particularly focused on the supply of (1) the precursor molecules and (2) electrons to the deposition spot because these determine the surface reactions.

To reveal the fundamental mechanism that governs the formation of elongated single-crystal Au SNPs, the inner structure of the NPs was studied by HR(S)TEM. In Figure 3a,b, a detailed view of the top and middle parts of a NP shows a gradual increase of the average crystallite size toward the bottom of the NP. In particular, a paraboloid-shaped boundary between the top and middle sections is clearly visible some 70 nm from the top, where the size and density of the crystallites increases quite abruptly, from ∼4 nm in the upper part to ∼7 nm in the lower part. As one proceeds down the NP, the crystallites appear to form increasingly larger lumps ranging from ∼10 to ∼30 nm in size, which are continuously present throughout the lower parts of the NP. These structural features indicate that, apart from the role of precursor molecule supply, one needs to consider the impact of the electron beam on the underlying NP sections.

To model the propagation of a 3 keV electron beam in such a vertically growing nanostructure, we used *CASINO* Monte Carlo simulation software.[39] Like in our experiments, the electron beam impinged on a model NP in the direction of its vertical (i.e., height) axis. For the simulations (Figure 3c), a 1.1 μm tall model NP was created by stacking 100 cylindrical slices, with each being 11 nm in thickness and 100 nm in diameter. Using our standard deposition parameters, such a slice would be experimentally deposited within ∼0.5 s. Relying on our experimental findings (Figure 2), the model NP considers a gradual increase in the Au content by 1 atom % per slice, starting from the top, which contained 1 atom % of Au. The remainder was a nonmetallic material consisting of C and O in a (local) relative atomic ratio of 85:15. Such a model was found to closely resemble the actual chemical composition of FEBID Au NPs, as observed by STEM−EDX. In the model NP, the maximum penetration depth of 3 keV electrons was ∼110 nm (Figure S6 in the SI), with less than 0.5% of primary electrons penetrating more than 100 nm into the material. This result suggests that during deposition the primary electrons impinging on the actual top section of the growing NP are also able to reach the already deposited lower sections of the NP, where they can dissipate their 3 keV energy, mainly by inelastic scattering and Joule heating. We note that the model assumed a homogeneous distribution of Au atoms within each cylindrical slice of the model NP, whereas in reality the Au atoms are agglomerated as nanocrystallites that are embedded in a carbonaceous matrix; hence, the real penetration depth of electrons is expected to be somewhat different from the value of 110 nm obtained by simulations in a homogeneous material. In conclusion, the simulation shows that, within the constantly growing NP, the major part of the primary electron energy is dissipated within less than 100 nm from the top. Because of the constant growth of the NP, the highest accumulated dose of electrons is always received at the penetration boundary and all sections below. In the calculated model, the total electron dose on the NP sections below ∼110 nm from its top reaches saturation at $\sim 2 \times 10^7$ e nm^{-2}. The penetration depth and profile of the beam (Figure 3c) may explain the observed feature identified as the curing front. Because the primary electrons also reach center portions of the NP, they can trigger structural changes in the already deposited material. In addition, heating of the NP can be expected because of dissipation of the primary electron energy within the NP as well as current flowing through the NP into the substrate (Joule heating).[40,41]

On the basis of the simulation results, it seems reasonable that the electron beam (which is primarily utilized for deposition) has an extra role in the growth process: it cures the previously deposited material during the growth of top sections. We therefore propose that the primary electrons from the beam generate secondary electrons that crack some of nondecomposed (or only partially decomposed) Au precursor molecules trapped on or within the NP and increase diffusion, leading to the formation of Au crystallites. This may explain the Au concentration gradient along the NP. In addition, by this energy uptake and Joule heating, larger Au crystallites are formed by coalescence of smaller Au particles (and individual atoms) within the carbonaceous matrix. A similar effect of coagulation was observed in FEBID platinum (Pt) material subjected to postgrowth electron-beam curing[42−45] or in situ laser heating.[29] This corresponds to the observed difference in the crystal size between the topmost ∼70 nm section and the middle section. During the atomic rearrangement and additional cracking of trapped precursor molecules (or ligands), some C- and oxygen (O)-containing species (1) are likely diffusing to the surface, are directly released from the deposit in the gaseous phase, and are pumped away by the experimental system or (2) are oxidized to CO_x by the water vapor in the vacuum chamber (which is typically present at a background pressure of 1.6×10^{-6} mbar)[46] so that the oxidized products are pumped away. Hence, diffusion, direct desorption, and surface oxidation may also lead to Au-richer material, as evidenced by EDX.

On the basis of these experimental and simulation results, we propose FEBIC as the underlying process for the observed autopurification. Within FEBIC, the electron beam performs in situ curing of the material during deposition of a vertical NP and supports the detachment and release of gaseous C- and O-containing species.

To reject or verify the FEBIC hypothesis, the proposed mechanism was compared to existing knowledge. First, the proposed mechanism is substantiated by previously reported

DOI: 10.1021/am507327y
ACS Appl. Mater. Interfaces 2015, 7, 2467−2479

direct observations that electron irradiation of Au nanocrystallites on carbonaceous substrates leads to their restructuring.[47−49] Second, the validity of the FEBIC hypothesis can be tested indirectly by assessing the electrical properties of the FEBID Au material. In this notion, the higher electron doses used during deposition should lead to a higher purity and larger crystal grains and, consequently, a lower electrical resistivity ρ. Indeed, previously it was experimentally found that the resistivity of pristine FEBID Au structures depended on the electron-beam current used for FEBID.[11] A corresponding behavior has been observed for pristine FEBID cobalt (Co) and Pt nanostructures,[40,43] as well as for postgrowth cured FEBID Pt and copper NPs.[44,45,50,51] We think that all of these observations are different manifestations of the same fundamental principle: in situ FEBIC. Taking that into account, we performed three additional experiments to empirically test the FEBIC hypothesis and to gain further insight into its mechanism.

If an electron beam really does modify the FEBID Au material, this effect should occur whenever the electron beam is applied. Hence, *the first key experiment* was designed to investigate postgrowth curing. For this purpose, we used the top section of a FEBID Au NP because this "youngest" section of the NP had experienced the lowest electron dose during deposition.

A controlled postdeposition electron-beam treatment of the NP tip was performed simultaneously with imaging inside a 200 keV TEM over a period of 30 min. The TEM beam intensity and exposure time were carefully set to give a total integrated electron dose of $\sim 2 \times 10^7$ e nm^{-2}, which was identical with the dose experienced by the middle and bottom sections of the NP during the previous deposition process by SEM. The effect of 200 keV electron irradiation on the NP tip was directly monitored by TEM in real time. Figure 4 summarizes the observed behavior of a FEBID Au NP before and after electron beam exposure: initially smaller Au crystallites (3−6 nm) over time formed larger crystallites (10−20 nm). Despite this significant structural transformation, electron irradiation did not lead to an apparent volume shrinkage of the NP, contrary to expectation based on the reported case of electron irradiation of FEBID Pt NPs.[45] STEM−EDX measurements showed no detectable long-range (>10 nm) compositional change in the irradiated sections. Furthermore, the postdeposition TEM electron-beam curing experiments never induced a lateral growth of SNPs or larger single crystals on the top sections of Au NPs, regardless of the electron intensity or dose used. These observations in the TEM confirm the coalescence of Au crystallites but cannot explain the increased Au purity and the emergence of SNPs in the bottom section of the NP. We propose that the latter effects are related to simultaneous processes depending on the specific process parameters during FEBID by SEM. For this reason, we compared the corresponding experimental conditions.

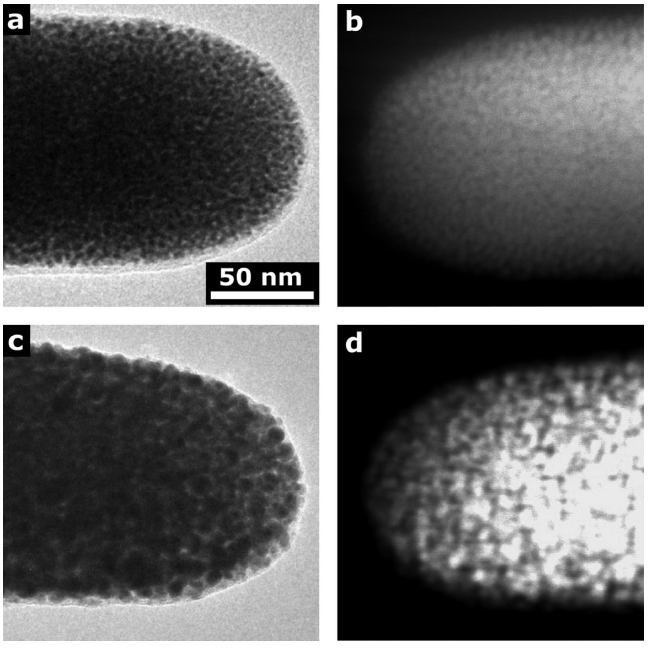

Figure 4. BF-TEM (a and c) and HAADF-STEM (b and d) images of the top section of a FEBID Au NP before (a and b) and after (c and d) 200 keV electron irradiation with a dose of 2×10^7 e nm^{-2}. The scale bar applies to all images. Coarsening of Au nanocrystallites is clearly visible, but no SNPs are formed during irradiation.

The main differences between simultaneous curing of the bottom section and postdeposition curing of the top section are (1) the use of high-energy 200 keV electrons instead of 5 keV electrons, (2) the ultrahigh vacuum conditions, and (3) the absence of Au precursor during postdeposition TEM curing.

First, the different interaction of the high energy of 200 keV primary electrons of a TEM with FEBID NPs yields a much lower secondary electron density compared to the 5 keV primary electrons studied by Porrati et al,[45] or compared to the 3 keV primary electrons of a scanning electron microscope used for the described deposition of NPs (Figures 2 and 3). However, the previously postulated mechanism of the electron-triggered chemical decomposition of Au precursor molecules, that are trapped on or within the NP, requires electron energies on the order of several electronvolts, which happens to be the typical energy range of secondary electrons. Because 200 keV electrons yielded far fewer secondary electrons in the suitable energy range, no significant change of the chemical composition could be expected: consequently, no postpurification effect was observed in this TEM experiment. Furthermore, other effects of high-energy electron irradiation, such as heating by inelastic scattering or Joule heating, occurred at a significantly larger spatial scale than that when low-energy electrons are used.

Second, water vapor and oxygen, typically present in the background atmosphere of a scanning electron microscope, are now scarce in the TEM column. This deficiency of an oxidizing species may (partially) be responsible for the absence of purification effects.

Third, the lack of any Au precursor during postgrowth curing coincides with an unchanged Au content in the NPs and with the total absence of SNPs. The result in Figure 4 strongly suggests that, in a relatively pure TEM atmosphere, the 200 keV electron beam alone cannot cause the formation of elongated SNPs on predeposited FEBID structures.

Because the growth of SNPs only occurs during deposition in the presence of the Au precursor and only up to a height of ~400 nm from the substrate, we consider two mechanisms as most conceivable: either inelastic scattering of the primary electron beam within the NP (or on the substrate) promotes the growth of newly formed larger Au crystallites (including sideway growth) from the fresh Au precursor or this deposition process of Au precursor may be thermally triggered by heating of the NP. In the case of Joule heating of the NP, the bottom

DOI: 10.1021/am507327y
ACS Appl. Mater. Interfaces 2015, 7, 2467−2479

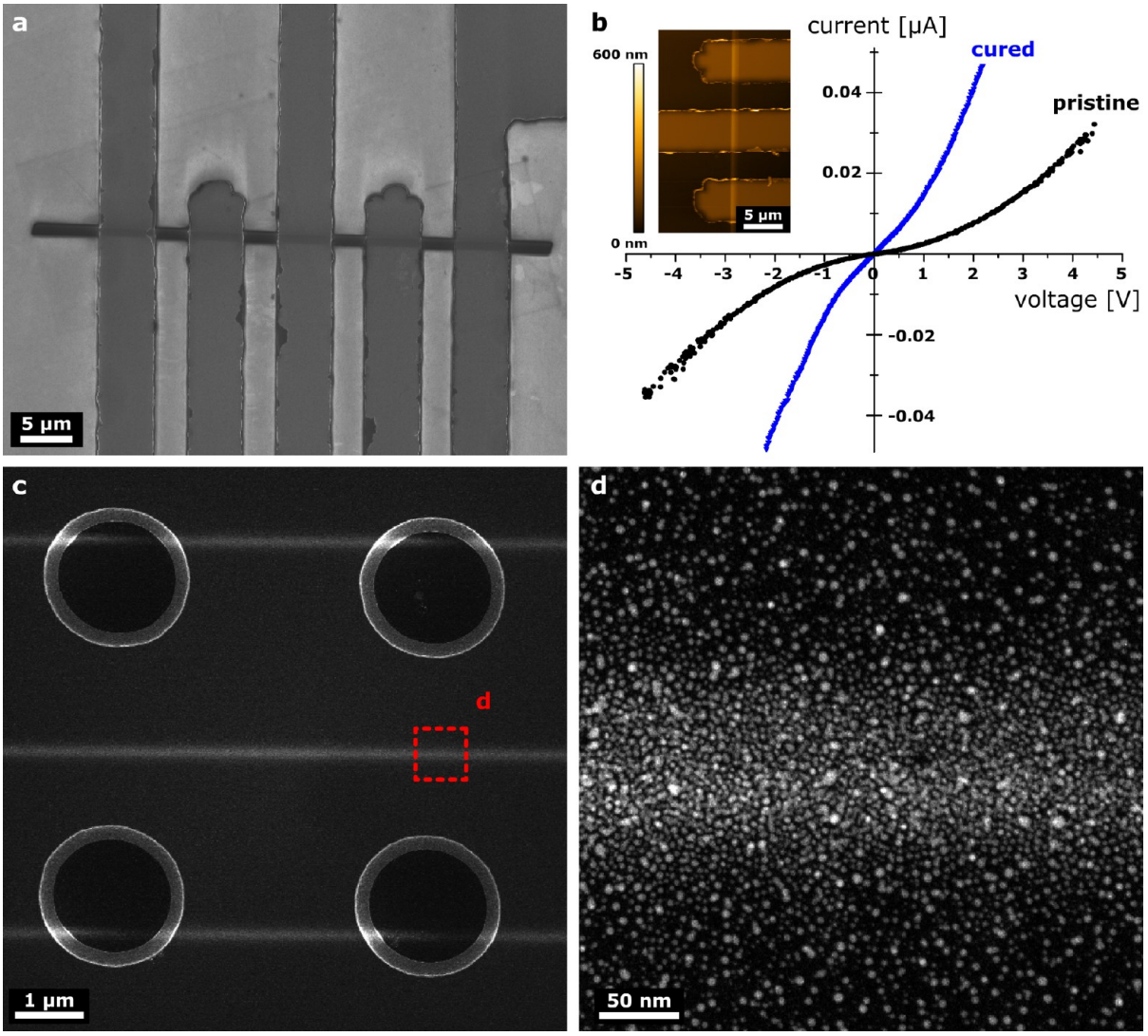

Figure 5. (a) Top-view SEM image of a pristine FEBID Au NW prepared for five-point probe electrical measurements. (b) Corresponding $I-V$ characteristics before ("pristine") and after ("cured") electron-beam irradiation with a dose of ~6.8×10^3 e nm^{-2}. Inset: AFM image of the NW. (c) HAADF-STEM image of pristine FEBID Au NWs deposited onto a perforated silicon nitride TEM membrane. The dashed square indicates the part of the NW that was investigated in detail. (d) Close-up HAADF-STEM image of the NW showing nonpercolating Au nanocrystallites.

section will be the hottest because it experiences the longest continuous electron current flowing from the NPs into the substrate. At the same time, this NP section has the highest Au precursor coverage as the precursor diffuses from the substrate toward the top of the NP (adsorption from the gas phase will be approximately equal in all sections). Hence, to initiate the growth of new Au crystallites, it is reasonable that the growth of SNPs is dependent on the supply of fresh precursor molecules. With postdeposition curing in a TEM, this necessary condition was not fulfilled and consequently no SNP was formed.

It may be further speculated that SNPs are produced by a combination of electron-beam curing of the material during FEBID and catalytic decomposition of Au precursor molecules on the freshly purified Au crystallites acting as nucleation sites for SNP growth. This notion seems plausible because the catalytic activity of Au is well-known[52] and autocatalytic deposition has been reported in the case of FEBID iron and chromium nanostructures.[53,54]

The second key experiment was designed to confirm the curing effect by comparing the electrical properties of pristine FEBID Au nanostructures before and after FEBIC. If the proposed FEBIC mechanism governs the coalescence of small Au particles and also has a purifying effect, then the Au nanostructures should have a higher conductivity after FEBIC. For electrical characterization of FEBID material, we performed conductivity measurements because it was expected that such experiments could implicitly reveal the changes in the structure and composition of the deposits. Namely, it is known that the electrical conductivity of the FEBID Au material depends on the deposition parameters: primarily on the electron-beam current,[8,10] beam dwell time, and pixel-to-pixel spacing used for deposition. Our experiments indicate that these parameters tailor the simultaneous curing process during FEBID (see Figures 3 and 4): it appears that, depending on the experimental deposition parameters used, the structure and, hence, conductivity of the FEBID Au material may vary significantly. So, instead of comparing the absolute conductivity of different FEBID structures (and risking systematic errors), we studied the relative change of the conductivity of the nanostructures subjected to controlled postdeposition FEBIC.

DOI: 10.1021/am507327y
ACS Appl. Mater. Interfaces 2015, 7, 2467−2479

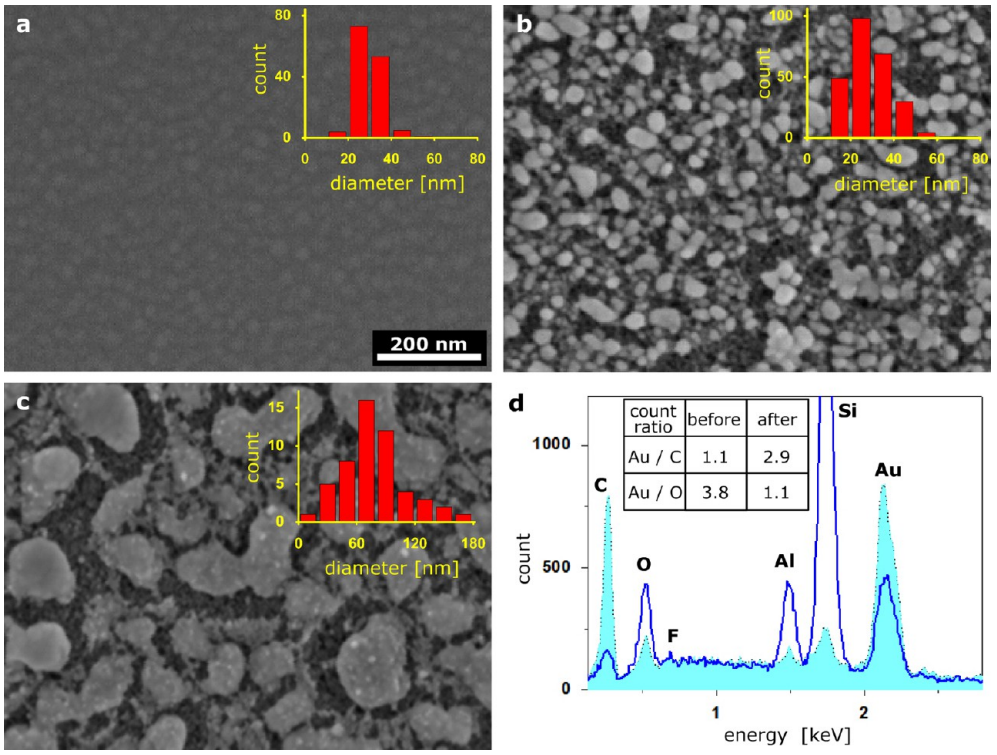

Figure 6. Top-view SEM images of a planar FEBID Au: (a) pristine structure; (b) oxygen-plasma-treated (t = 60 s) structure; (c) FEBIC (9.4×10^3 e nm^{-2}) + oxygen-plasma-treated (t = 60 s) structure. The scale bar applies to all images. Inset: Corresponding Au crystallite size distribution, with crystallite sizes of 28.8 ± 0.6, 29.6 ± 0.5, and 79 ± 4 nm, respectively. (d) EDX spectra of the planar FEBID Au sample before (dotted line) and after (solid line) oxygen plasma treatment, indicating a significant decrease of the C content in the deposit. The Si, Al, and (partially) O peaks originate from the substrate, while the F signal (possible precursor residue) appears to be indistinguishable from the measurement noise.

For that reason, we deposited lateral FEBID Au NWs across the contacts of lithographically patterned five-point probes and measured the current−voltage (I−V) characteristics (see Figure 5). The current values were set low enough ($\ll$1 μA) to ensure that we were far from critical current densities, thus avoiding electromigration or Joule thermal annealing of the NWs during electrical measurement. As shown in Figure 5b, at such low currents the pristine FEBID Au NWs exhibit the typical characteristics of tunneling conductance[55] following the power-law dependence $I \sim (V - V_t)^{\zeta}$, with the experimentally obtained value of $\zeta = 2.3 \pm 0.2$. This is in good correlation with the observed structure because the pristine material comprised individual nonpercolating Au nanocrystals embedded in an amorphous carbonaceous matrix, as is evident from the HAADF-STEM images of FEBID Au NWs (Figure 5c,d). It is worth noting that the sections of the NWs that were deposited over thinner circular areas of the perforated membrane contained significantly less material than the sections deposited over the remaining thicker part of the membrane, demonstrating the effect of the substrate thickness on FEBID.[56] Atomic force microscopy (AFM) measurements were conducted to obtain more accurate cross-sectional profiles of the analyzed NWs, so the specific resistivity ρ could be calculated. The specific resistivity of the pristine lateral Au NWs was found to be $\rho \sim 5\ \Omega$ cm, which is a feature of a relatively poor conductor.

In the next step, the pristine NWs were then briefly (60 s) exposed in a scanning electron microscope (background pressure of 1.6×10^{-6} mbar; no Au precursor added) to 5 keV electron irradiation, with a total dose of ~6.8×10^3 e nm^{-2}. Even such a relatively gentle FEBIC caused the Au NWs' resistivity to drop considerably, by a factor of 5 (see Figure 5b), while still showing the I−V behavior typical for the tunneling regime. On the basis of the results of TEM curing of free-standing FEBID NPs (Figure 4), we reason that a similar coarsening of Au nanocrystallites took place here in the case of SEM curing of lateral FEBID NWs. Notably, the measured increase in the tunneling current through the FEBID Au NWs is in perfect agreement with the previously observed decrease of the spacing distance between Au nanocrystallites during TEM curing. The same behavior was repeatedly observed on other cured FEBID Au NWs that were deposited using different experimental parameters (e.g., dwell time and number of loops). The increase of the conductivity after FEBIC strongly supports the hypothesis that electron-beam curing conditions (such as the current and accelerating voltage) can successfully tailor the electrical conductivity of FEBID Au structures. This mechanism seems valid both for in situ FEBIC during FEBID and for common postdeposition curing.

As third and final key experiment to test the FEBIC hypothesis, the curing process was also used on a planar (lateral) nanostructure. Planar FEBID area deposition is often used for making prototype nanoelectronic devices, where the properties of the deposited material strongly influence the features of the device. However, the geometry of thin-layer deposits results in (1) a different electron interaction not directly comparable to vertical NPs, (2) reduced heating of the deposit due to a larger substrate interface area, (3) a different precursor supply (including precursor diffusion), and (4) a different supply of residual gases such as water. Therefore, an appropriate method for curing of the planar structures must be established separately from the curing of vertical NPs. We

DOI: 10.1021/am507327y
ACS Appl. Mater. Interfaces 2015, 7, 2467−2479

investigated whether FEBIC of the planar structures also leads to changes of their granularity and purity, which may consequently alter their electrical characteristics. For this reason, the size distribution of Au nanocrystallites was measured before and after postdeposition FEBIC. To expose the Au nanocrystallite distribution, FEBIC curing was coupled with a subsequent oxygen plasma treatment, acting as a postdeposition purification process that removes the carbonaceous components off the deposit. With this experiment, for the first time, the combination of FEBIC and postdeposition purification was evaluated as a novel route to gain planar nanostructures with a high Au content, which by far exceeds the Au fraction in pristine FEBID.

Postdeposition purification has already been a major topic of the FEBID community for decades, and a range of postdeposition purification methods have been investigated,[57] including electron-beam-assisted purification using oxygen[58] or water vapor,[42] oxygen treatment at elevated temperatures,[24,32] laser annealing in oxygen,[59] vacuum thermal annealing,[60] or annealing in air.[31] Specifically, argon–hydrogen microplasma treatment showed promising results,[61] but the custom-built apparatus restricted its widespread usage. Here we demonstrate that a significant increase of the metallic content in FEBID Au structures can be achieved using a common laboratory oxygen plasma reactor.

Independent of any postdeposition process, we already showed for NPs (Figure 2c) that the optimization of experimental FEBID parameters alone yielded pristine Au nanostructures of increased purity (with the local Au content at the bottom sections readily reaching >50 atom %). In addition, we demonstrated that postdeposition electron irradiation causes coarsening of Au nanocrystallites within FEBID Au material (Figure 4). Both of these results can be attributed to the proposed FEBIC mechanism. If this mechanism really exists, then now we intend to take advantage of the curing behavior: we propose to purify planar FEBID Au nanostructures by combining postdeposition FEBIC (which according to our model would lead to coarsening of Au crystallites) with oxygen plasma treatment (which will additionally remove the carbonaceous matrix).

To study such a cleaning procedure, relatively large planar FEBID Au structures (>100 μm^2) of ∼60 nm thickness were deposited onto a Si substrate. In the first step, before oxygen plasma treatment, only selected areas of the pristine planar FEBID Au structures (Figure 6) were additionally subjected to postdeposition FEBIC by being exposed to 5 keV SEM electron irradiation with a relatively small dose of $\sim 9.4 \times 10^3$ e nm^{-2}. In the next step, the carbonaceous matrix from the FEBID material was removed by oxygen plasma treatment of the samples. As shown in Figure 6c,d, the oxygen plasma treatment visibly changed the surface morphology of both the pristine (noncured) and cured FEBID Au material: removal of the carbonaceous matrix exposed its inner granular structure and made it accessible for clear SEM imaging. On the downside, oxygen plasma treatment may increase the O content in the treated samples, supposedly because of the incorporation of O atoms into the sample. For chemical analysis of the electron-beam-cured and -noncured areas, several EDX spectra were taken on 2×2 μm^2 areas after oxygen plasma purification. These EDX spectra indicate a considerable (∼60%) decrease in the C content (see Figure 6d): while the pristine FEBID Au structures typically had a relative atomic ratio of Au:C = 1:2, the samples treated with oxygen plasma for 60 s exhibited a ratio of Au:C = 11:9. We also note that the final composition depended on the duration of the plasma cleaning procedure; e.g., it reached a ratio of Au:C = 2:1 in the samples that were oxygen-plasma-cleaned for a longer duration of 180 s (not shown), resulting in a 75% reduction of C. In general, we noticed that the C removal efficiency was not linearly proportional to the period of cleaning: the amount of C removed in the initial stages (<60 s) was much higher than the amount removed in the final stages (e.g., in the period 120–180 s). This is reasonable if the Au grains in the area deposition are initially coated by a carbonaceous material (as was also observed with Au NPs; see Figure 2a), while in later stages of oxygen plasma treatment, the exposed Au grains effectively act as masks for removal of the underlying carbonaceous material, so the C species can only be removed from the gaps between the Au grains. A stable level of the Au content (Au:C ∼ 5:2) was reached after ∼300 s of oxygen plasma treatment when the exposed Au grains completely shielded the underlying carbonaceous matrix from further oxidation by the reactive oxygen plasma, inhibiting any further C removal.

Interestingly, the morphology of FEBID Au structures that had additionally been exposed to FEBIC (Figure 6c) appeared to be quite different after oxygen plasma treatment than the morphology of the unexposed parts (Figure 6b). Coalescence of Au crystallites was much more pronounced in the FEBIC parts of the structures than in the non-FEBIC parts. We conclude that the postgrowth electron irradiation strongly impacted the inner structure of the FEBID Au material and has led to a major redistribution of Au atoms and nanocrystallites within the carbonaceous matrix. What is more, the effect of this 60 s FEBIC by a 5 keV SEM beam (Figure 6c) was seemingly even more pronounced than that in the case of 30 min FEBIC of Au NPs by a 200 keV TEM beam (see Figure 4). We also note that the presence of a bulk substrate may have impacted the number of generated backscattered and secondary electrons.[62] These observations further support our assumption that low-energy secondary electrons are the main contributor for structural and chemical changes in FEBIC Au nanostructures. In addition, after FEBIC, the cured areas clearly exhibit more connections between larger grains. Compared to the pristine unexposed material, FEBIC has created an almost completely percolating network of larger Au crystallites, with the carbonaceous matrix filling the now enlarged distances between the larger Au grains. Such a structure of linked larger crystallites is very likely more conductive than a structure of individual smaller nanocrystallites having far fewer interconnects. The pronounced percolation present in the FEBIC Au material is consistent with the previously performed electrical conductivity measurements: the observed 5-fold increase in the conductivity of the FEBIC samples over the pristine FEBID Au NWs (Figure 5b) perfectly correlates with the structural changes (percolation) induced by FEBIC, which were revealed to SEM imaging only by postdeposition oxygen plasma cleaning (Figure 6). Similar to the first curing experiment of Au NPs in the TEM (Figure 4), SEM curing of planar areas only changed the structure, whereas the average elemental composition over a broad cured area (Figure 6c) remained almost identical with the one in the unexposed parts of the sample (Figure 6b). This result indicates that FEBIC is the right approach to tailoring the structural properties of the FEBID Au material. Oxygen plasma cleaning exposed the buried Au nanocrystallites and revealed pronounced coalescence of Au nanocrystallites inside the cured FEBID Au

DOI: 10.1021/am507327y
ACS Appl. Mater. Interfaces 2015, 7, 2467–2479

material. The experiments on planar deposits clearly illustrate the effect of electron-induced curing and confirm the proposed curing model. Additionally, these results openly demonstrate the effectiveness of oxygen plasma cleaning of FEBID Au nanostructures for both pristine and electron-beam-cured deposits. It has to be stressed that by a combination of these two approaches, for the first time, a technologically feasible process producing Au-rich planar deposits is introduced, which could be beneficial for numerous applications.

We have proposed FEBIC as a new mechanism present during FEBID and have clearly supported this model by three key experiments. FEBIC has been presented as a method to modify the structural and electrical properties of FEBID Au nanostructures. It was shown experimentally that both the low-energy SEM and high-energy TEM electron beams are capable of performing postgrowth curing of FEBID Au deposits. Moreover, our experimental results indicate that the FEBIC mechanism is inherently involved in FEBID and always occurs simultaneously with deposition: electron-beam curing in a scanning electron microscope led to a radical increase in the Au content in FEBID NPs, which gradually increased from ∼25 atom % (top section) to >70 atom % (bottom section), with a maximum of ∼90 atom % found in single-crystal SNPs.

However, electron-beam curing alone did not explain the growth of the observed elongated single-crystal SNPs. For the growth of elongated SNPs, sufficient fluxes not only of electrons but also of precursor molecules at the deposition site seem to be crucial. Additionally, thermal effects that are undividedly linked to the interaction of electrons with matter were considered. As a direct effect of electron irradiation, (1) an increase of the local temperature at the nucleation site and (2) Joule heating as a consequence of the current flowing through the NP may be expected: these thermal effects could facilitate the growth of SNPs.

Finally, on the basis of our experimental results, we propose the following three necessary conditions for lateral growth of SNPs: (1) the formation of a sufficiently large single-crystal Au as a nucleation site, where FEBIC of the FEBID Au material plays a crucial role, then (2) surface exposure of the Au clusters by desorption or oxidation of surface carbonaceous species, and finally (3) a sufficient supply of secondary electrons and precursor molecules to these nucleation sites for the growth of elongated SNP, as illustrated in Figure 7. The proposed model for SNP growth is fully consistent with all of our experimental observations: NPs that have SNPs tend to have many larger Au crystallites at the base, while those NPs that do not have pronounced SNPs (but only lumps) have significantly less or no larger crystallites at their base. This indicates the necessity of a larger Au crystallite to act as a nucleation site for SNPs. The necessity of a sufficient precursor supply is further emphasized by the fact that SNPs originate only at the bottom ∼400 nm section of the NPs and, when formed, extend sideways up to a total length of ∼300 nm. The absence of SNPs in higher sections of NPs suggests that either a limited supply of secondary electrons or a limited supply of precursor molecules via surface diffusion hinders any further SNP growth. The supply of a precursor by surface diffusion is especially relevant in the present experiment because (1) the spot deposition of NPs by continuous, uninterrupted electron exposure favors a precursor limited growth regime and (2) the precursor adsorption on the NP's tip directly from the gas phase alone cannot provide enough precursor molecules for the observed growth rate. Experimental evidence indicates that, although

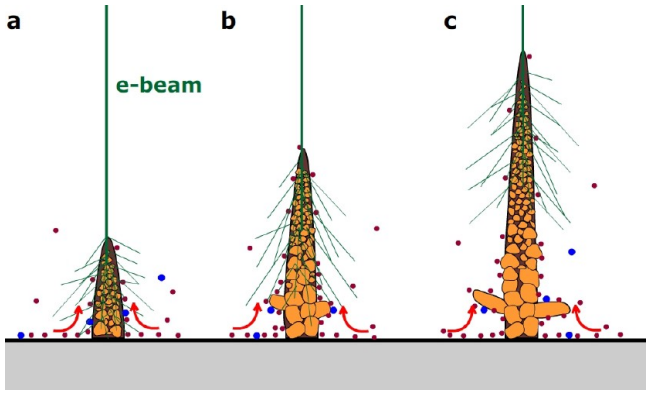

Figure 7. Schematics of the proposed FEBIC mechanism that yields Au NPs of high purity, displayed as subsequent NP growth stages. Primary electron trajectories are illustrated with lines. (a) Initially, growth is typically upward in the direction of the electron beam. The beam at the same time penetrates into the underlying parts, curing the deposited material. For sufficiently high electron doses, larger Au crystallites are formed. (b) As the growth continues, some of larger Au crystallites extend out of the vertical NP, forming SNPs. (c) SNPs grow laterally as long as there is a sufficient supply of secondary electrons, precursor molecules, and oxidizing species at the site.

larger Au crystallites did form in the upper sections of NPs, i.e., above ∼400 nm (see Figure 3), these nucleation sites were never observed to initiate the growth of SNPs for any set of experimental parameters used in our study.

CONCLUSIONS

In conclusion, direct fabrication of submicrometer–large pure Au crystallites within FEBID nanostructures has been demonstrated for the first time. Moreover, we have identified FEBIC (inseparably entangled with FEBID) as the underlying mechanism responsible for the observed increase of the Au content. Additionally, standard oxygen plasma treatment has been used as novel postdeposition cleaning procedure to further boost the Au content in FEBID planar deposits. We note that an appropriate combination of FEBID, FEBIC, and postdeposition oxygen plasma cleaning may lead to the direct deposition of pure crystalline Au nanostructures from common metal–organic precursors. The proposed FEBIC mechanism and subsequent approaches can relieve FEBID Au structures from the traditionally low Au content and open new application areas for FEBID Au nanomaterials.

METHODS

Au-containing samples were fabricated by using FEBID from the dimethylgold(III) trifluoroacetylacetonate precursor (molecular formula $C_7H_{10}AuF_3O_2$, CAS no. 63470-53-1). Deposition was performed inside an oil-free Zeiss Leo 1530VP scanning electron microscope equipped with a homemade gas injection system (GIS).[15] The Au precursor was maintained at an elevated temperature of 55 °C in the reservoir of a miniaturized custom-tailored heatable GIS. The nozzle was a straight cylindrical tube with an inner diameter of 400 μm and was adjusted to a 55° tilt angle at a distance of 300 μm above the substrate surface. From a total injected precursor flux of 6×10^{16} molecules s^{-1}, the actual impingement rate of the deposition region located roughly 1 mm away from the center of the nozzle aperture was less than 1% of the total flux.[63] The base pressure (without precursor) of the deposition chamber was 1.6×10^{-6} mbar, while the working pressure during deposition (with the precursor line opened) was maintained at 1.2×10^{-5} mbar. While the directional precursor gas flux from the nozzle is magnitudes higher, the background pressure

DOI: 10.1021/am507327y
ACS Appl. Mater. Interfaces 2015, 7, 2467–2479

(mainly caused by residual water vapor)[46] provides an exposure of 1.2 langmuir s^{-1} and the system pressure (mainly caused by the Au precursor) provides an additional exposure of 7.8 langmuir s^{-1}. Hence, in the fastest case (assuming a theoretical sticking coefficient of 1 for all involved gases), monolayer coverage is achieved within 111 ms with 13% of the coverage originating from the background pressure. Although a wide experimental parameter space was explored (see the SI), all Au structures shown in the paper were deposited using a 3 keV electron beam with a current of 1 nA. The vertical NPs were deposited using customized macros written in the *SmartSEM* interface, whereas the horizontal NWs and planar structures were fabricated using a Raith Elphy Plus pattern generator.

The free-standing NPs used for SEM characterization were deposited onto an ultrasonically cleaned p-type Si substrate having a native oxide of ∼2 nm,[19] while the free-standing NPs used for TEM characterization were deposited onto an inclined Si window TEM grid (Figure S3 in the SI). The horizontal NWs used for structural and compositional characterization were deposited onto the frame window of a perforated silicon nitride TEM membrane purchased from SPI Supplies, while the horizontal NWs used for electrical characterization were deposited onto thermally grown silicon oxide substrates (thickness >100 nm) having lithographically produced electrical five-point probes (50-nm-thick Au on 5-nm-thick titanium). The planar samples were deposited onto an atomic layer deposition thin film (<20 nm) of alumina.

SEM characterization and electron-beam curing experiments were conducted in a Zeiss Neon 40EsB cross-beam microscope at a base pressure of 1.3×10^{-6} mbar and a 5 kV acceleration voltage. EDX was performed at 5 kV using an Oxford Instruments EDS 7427 detector. TEM characterization was carried out using a FEI Tecnai TF20 microscope equipped with an EDAX detector for EDX and a Fischione 3000 detector for high-angle annular dark-field imaging, at an acceleration voltage of 200 kV. Five-point probe electrical characterization of horizontal NWs was performed using an Agilent 4155B semiconductor parameter analyzer. AFM measurements were conducted using a Veeco/Bruker Dimension 3000 atomic force microscope in the tapping mode. Oxygen plasma treatment of deposited structures was performed in a Tepla 100 plasma system at a power of 300 W and an oxygen pressure of 1 mbar. The samples for SEM analysis were briefly exposed (<2 min) to cleanroom air during transfer from the Zeiss Leo 1530VP scanning electron microscope or Tepla 100 plasma system to the Zeiss Neon scanning electron microscope. The samples for TEM characterization were exposed to the atmosphere for a few hours during the transfer from the cleanroom to the TEM laboratory. SEM and TEM images were analyzed using *ImageJ* software.

■ ASSOCIATED CONTENT

Ⓢ Supporting Information

Additional SEM (Figures S1−S3), TEM (Figures S4 and S5), and Monte Carlo simulation data (Figure S6). This material is available free of charge via the Internet at http://pubs.acs.org.

■ AUTHOR INFORMATION

Corresponding Author

*E-mail: heinz.wanzenboeck@tuwien.ac.at.

Present Address

‡D.B.: Department of Chemistry, University of Liverpool, Crown Street, Liverpool L69 7ZD, United Kingdom.

Author Contributions

The manuscript was written through contributions of all authors. All authors have given approval to the final version of the manuscript.

Notes

The authors declare no competing financial interest.

■ ACKNOWLEDGMENTS

The research was funded through the European Community's Seventh Framework Program (FP7/2007-2013) under Grant ENHANCE-238409 and the Austrian Science Fund Project P24093 and supported by the Center for Micro- and Nanostructures at the Vienna University of Technology. TEM characterization was carried out using facilities at the USTEM at Vienna University of Technology.

■ REFERENCES

(1) Wnuk, J. D.; Rosenberg, S. G.; Gorham, J. M.; van Dorp, W. F.; Hagen, C. W.; Fairbrother, D. H. Electron Beam Deposition for Nanofabrication: Insights from Surface Science. *Surf. Sci.* **2011**, *605*, 257−266.

(2) Utke, I.; Hoffmann, P.; Melngailis, J. Gas-Assisted Focused Electron Beam and Ion Beam Processing and Fabrication. *J. Vac. Sci. Technol. B* **2008**, *26*, 1197−1276.

(3) van Dorp, W. F.; Hagen, C. W. A Critical Literature Review of Focused Electron Beam Induced Deposition. *J. Appl. Phys.* **2008**, *104*, 081301−081342.

(4) van Dorp, W. F.; Zhang, X.; Feringa, B. L.; Hansen, T. W.; Wagner, J. B.; De Hosson, J. T. M. Molecule-by-Molecule Writing Using a Focused Electron Beam. *ACS Nano* **2012**, *6*, 10076−10081.

(5) Mølhave, K.; Madsen, D. N.; Dohn, S.; Bøggild, P. Constructing, Connecting and Soldering Nanostructures by Environmental Electron Beam Deposition. *Nanotechnology* **2004**, *15*, 1047.

(6) Madsen, D. N.; Mølhave, K.; Mateiu, R.; Rasmussen, A. M.; Brorson, M.; Jacobsen, C. J. H.; Bøggild, P. Soldering of Nanotubes onto Microelectrodes. *Nano Lett.* **2003**, *3*, 47−49.

(7) Koops, H. W. P.; Weiel, R.; Kern, D. P.; Baum, T. H. High-Resolution Electron-Beam Induced Deposition. *J. Vac. Sci. Technol. B* **1988**, *6*, 477−481.

(8) Utke, I.; Dwir, B.; Leifer, K.; Cicoira, F.; Doppelt, P.; Hoffmann, P.; Kapon, E. Electron Beam Induced Deposition of Metallic Tips for Microelectronics Applications. *Microelectron. Eng.* **2000**, *53*, 261−264.

(9) Koops, H. W. P.; Schossler, C.; Kaya, A.; Weber, M. Conductive Dots, Wires, and Supertips for Field Electron Emitters Produced by Electron-Beam Induced Deposition on Samples Having Increased Temperature. *J. Vac. Sci. Technol. B* **1996**, *14*, 4105−4109.

(10) Weber, M.; Rudolph, M.; Kretz, J.; Koops, H. W. P. Electron-Beam Induced Deposition for Fabrication of Vacuum Field Emitter Devices. *J. Vac. Sci. Technol. B* **1995**, *13*, 461−464.

(11) Kretz, J.; Rudolph, M.; Weber, M.; Koops, H. W. P. Three-Dimensional Structurization by Additive Lithography, Analysis of Deposits Using TEM and EDX, and Application to Field-Emitter Tips. *Microelectron. Eng.* **1994**, *23*, 477−481.

(12) Fowlkes, J. D.; Doktycz, M. J.; Rack, P. D. An Optimized Nanoparticle Separator Enabled by Electron Beam Induced Deposition. *Nanotechnology* **2010**, *21*, 165303.

(13) Burbridge, D. J.; Crampin, S.; Viau, G.; Gordeev, S. N. Strategies for the Immobilization of Nanoparticles using Electron Beam Induced Deposition. *Nanotechnology* **2008**, *19*, 445302.

(14) Jenke, M. G.; Lerose, D.; Niederberger, C.; Michler, J.; Christiansen, S.; Utke, I. Toward Local Growth of Individual Nanowires on Three-Dimensional Microstrutures by Using a Minimally Invasive Catalyst Templating Method. *Nano Lett.* **2011**, *11*, 4213−4217.

(15) Hochleitner, G.; Steinmair, M.; Lugstein, A.; Roediger, P.; Wanzenboeck, H. D.; Bertagnolli, E. Focused Electron Beam Induced Deposition of Gold Catalyst Templates for Si-Nanowire Synthesis. *Nanotechnology* **2011**, *22*, 015302.

(16) Slingenbergh, W.; de Boer, S. K.; Cordes, T.; Browne, W. R.; Feringa, B. L.; Hoogenboom, J. P.; De Hosson, J. T. M.; van Dorp, W. F. Selective Functionalization of Tailored Nanostructures. *ACS Nano* **2012**, *6*, 9214−9220.

(17) Utke, I.; Jenke, M. G.; Roling, C.; Thiesen, P. H.; Iakovlev, V.; Sirbu, A.; Mereuta, A.; Caliman, A.; Kapon, E. Polarisation Stabilization of Vertical Cavity Surface Emitting Lasers by Minimally

DOI: 10.1021/am507327y
ACS Appl. Mater. Interfaces 2015, 7, 2467−2479

Invasive Focused Electron Beam Triggered Chemistry. *Nanoscale* **2011**, *3*, 2718−2722.
(18) Serrano-Ramón, L.; Córdoba, R.; Rodríguez, L. A.; Magén, C.; Snoeck, E.; Gatel, C.; Serrano, I.; Ibarra, M. R.; De Teresa, J. M. Ultrasmall Functional Ferromagnetic Nanostructures Grown by Focused Electron-Beam-Induced Deposition. *ACS Nano* **2011**, *5*, 7781−7787.
(19) Gavagnin, M.; Wanzenboeck, H. D.; Belić, D.; Bertagnolli, E. Synthesis of Individually Tuned Nanomagnets for Nanomagnet Logic by Direct Write Focused Electron Beam Induced Deposition. *ACS Nano* **2013**, *7*, 777−784.
(20) Shawrav, M. M.; Wanzenboeck, H. D.; Belić, D.; Gavagnin, M.; Schinnerl, M.; Bertagnolli, E. Mask-Free Prototyping of Metal-Oxide-Semiconductor Devices Utilizing Focused Electron Beam Induced Deposition. *Phys. Status Solidi A* **2014**, *211*, 375−381.
(21) Höflich, K.; Becker, M.; Leuchs, G.; Christiansen, S. Plasmonic Dimer Antennas for Surface Enhanced Raman Scattering. *Nanotechnology* **2012**, *23*, 185303.
(22) Graells, S.; Aćimović, S.; Volpe, G.; Quidant, R. Direct Growth of Optical Antennas Using E-Beam-Induced Gold Deposition. *Plasmonics* **2010**, *5*, 135−139.
(23) Graells, S.; Alcubilla, R.; Badenes, G.; Quidant, R. Growth of Plasmonic Gold Nanostructures by Electron Beam Induced Deposition. *Appl. Phys. Lett.* **2007**, *91*, 121112.
(24) Höflich, K.; Yang, R. B.; Berger, A.; Leuchs, G.; Christiansen, S. The Direct Writing of Plasmonic Gold Nanostructures by Electron-Beam-Induced Deposition. *Adv. Mater.* **2011**, *23*, 2657−2661.
(25) van Dorp, W. F.; Wu, X.; Mulders, J. J. L.; Harder, S.; Rudolf, P.; De Hosson, J. T. M. Gold Complexes for Focused-Electron-Beam-Induced Deposition. *Langmuir* **2014**, *30*, 12097−12105.
(26) Mulders, J. J. L.; Belova, L. M.; Riazanova, A. Electron Beam Induced Deposition at Elevated Temperatures: Compositional Changes and Purity Improvement. *Nanotechnology* **2011**, *22*, 055302.
(27) Mølhave, K.; Madsen, D. N.; Rasmussen, A. M.; Carlsson, A.; Appel, C. C.; Brorson, M.; Jacobsen, C. J. H.; Bøggild, P. Solid Gold Nanostructures Fabricated by Electron Beam Deposition. *Nano Lett.* **2003**, *3*, 1499−1503.
(28) Folch, A.; Tejada, J.; Peters, C. H.; Wrighton, M. S. Electron Beam Deposition of Gold Nanostructures in a Reactive Environment. *Appl. Phys. Lett.* **1995**, *66*, 2080−2082.
(29) Roberts, N. A.; Fowlkes, J. D.; Magel, G. A.; Rack, P. D. Enhanced Material Purity and Resolution via Synchronized Laser Assisted Electron Beam Induced Deposition of Platinum. *Nanoscale* **2013**, *5*, 408−415.
(30) Roberts, N. A.; Gonzalez, C. M.; Fowlkes, J. D.; Rack, P. D. Enhanced By-product Desorption via Laser Assisted Electron Beam Induced Deposition of $W(CO)_6$ with Improved Conductivity and Resolution. *Nanotechnology* **2013**, *24*, 415301.
(31) Riazanova, A. V.; Rikers, Y. G. M.; Mulders, J. J. L.; Belova, L. M. Pattern Shape Control for Heat Treatment Purification of Electron-Beam-Induced Deposition of Gold from the $Me_2Au(acac)$ Precursor. *Langmuir* **2012**, *28*, 6185−6191.
(32) Botman, A.; Mulders, J. J. L.; Weemaes, R.; Mentink, S. Purification of Platinum and Gold Structures after Electron-Beam-Induced Deposition. *Nanotechnology* **2006**, *17*, 3779.
(33) Brintlinger, T.; Fuhrer, M. S.; Melngailis, J.; Utke, I.; Bret, T.; Perentes, A.; Hoffmann, P.; Abourida, M.; Doppelt, P. Electrodes for Carbon Nanotube Devices by Focused Electron Beam Induced Deposition of Gold. *J. Vac. Sci. Technol. B* **2005**, *23*, 3174−3177.
(34) Utke, I.; Hoffman, P.; Dwir, B.; Leifer, K.; Kapon, E.; Doppelt, P. Focused Electron Beam Induced Deposition of Gold. *J. Vac. Sci. Technol. B* **2000**, *18*, 3168−3171.
(35) Plank, H.; Smith, D. A.; Haber, T.; Rack, P. D.; Hofer, F. Fundamental Proximity Effects in Focused Electron Beam Induced Deposition. *ACS Nano* **2011**, *6*, 286−294.
(36) Burbridge, D. J.; Gordeev, S. N. Proximity Effects in Free-Standing EBID Structures. *Nanotechnology* **2009**, *20*, 285308.
(37) Koops, H. W. P.; Kretz, J.; Rudolph, M.; Weber, M. Constructive Three-Dimensional Lithography with Electron-Beam Induced Deposition for Quantum Effect Devices. *J. Vac. Sci. Technol. B* **1993**, *11*, 2386−2389.
(38) Roediger, P.; Wanzenboeck, H. D.; Hochleitner, G.; Bertagnolli, E. Evaluation of Chamber Contamination in a Scanning Electron Microscope. *J. Vac. Sci. Technol. B* **2009**, *27*, 2711−2717.
(39) Demers, H.; Poirier-Demers, N.; Couture, A. R.; Joly, D.; Guilmain, M.; de Jonge, N.; Drouin, D. Three-Dimensional Electron Microscopy Simulation with the CASINO Monte Carlo Software. *Scanning* **2011**, *33*, 135−146.
(40) Utke, I.; Bret, T.; Laub, D.; Buffat, P.; Scandella, L.; Hoffmann, P. Thermal Effects During Focused Electron Beam Induced Deposition of Nanocomposite Magnetic-Cobalt-Containing Tips. *Microelectron. Eng.* **2004**, *73*−*74*, 553−558.
(41) Randolph, S. J.; Fowlkes, J. D.; Rack, P. D. Effects of Heat Generation during Electron-Beam-Induced Deposition of Nanostructures. *J. Appl. Phys.* **2005**, *97*, 124312−124318.
(42) Geier, B.; Gspan, C.; Winkler, R.; Schmied, R.; Fowlkes, J. D.; Fitzek, H.; Rauch, S.; Rattenberger, J.; Rack, P. D.; Plank, H. Rapid and Highly Compact Purification for Focused Electron Beam Induced Deposits: A Low Temperature Approach Using Electron Stimulated H_2O Reactions. *J. Phys. Chem. C* **2014**, *118*, 14009−14016.
(43) Plank, H.; Haber, T.; Gspan, C.; Kothleitner, G.; Hofer, F. Chemical Tuning of PtC Nanostructures Fabricated via Focused Electron Beam Induced Deposition. *Nanotechnology* **2013**, *24*, 175305.
(44) Plank, H.; Kothleitner, G.; Hofer, F.; Michelitsch, S. G.; Gspan, C.; Hohenau, A.; Krenn, J. Optimization of Postgrowth Electron-Beam Curing for Focused Electron-Beam-Induced Pt Deposits. *J. Vac. Sci. Technol. B* **2011**, *29*, 051801−051807.
(45) Porrati, F.; Sachser, R.; Schwalb, C. H.; Frangakis, A. S.; Huth, M. Tuning the Electrical Conductivity of Pt-Containing Granular Metals by Postgrowth Electron Irradiation. *J. Appl. Phys.* **2011**, *109*, 063715.
(46) Perentes, A.; Hoffmann, P. Oxygen Assisted Focused Electron Beam Induced Deposition of Si-Containing Materials: Growth Dynamics. *J. Vac. Sci. Technol. B* **2007**, *25*, 2233−2238.
(47) Lim, T. H.; McCarthy, D.; Hendy, S. C.; Stevens, K. J.; Brown, S. A.; Tilley, R. D. Real-Time TEM and Kinetic Monte Carlo Studies of the Coalescence of Decahedral Gold Nanoparticles. *ACS Nano* **2009**, *3*, 3809−3813.
(48) Buffat, P. A. Dynamical Behaviour of Nanocrystals in Transmission Electron Microscopy: Size, Temperature or Irradiation Effects. *Philos. Trans. R. Soc. London, Ser. A* **2003**, *361*, 291−295.
(49) Xue, B.; Chen, P.; Hong, Q.; Lin, J.; Tan, K. L. Growth of Pd, Pt, Ag and Au Nanoparticles on Carbon Nanotubes. *J. Mater. Chem.* **2001**, *11*, 2378−2381.
(50) Frabboni, S.; Gazzadi, G. C.; Felisari, L.; Spessot, A. Fabrication by Electron Beam Induced Deposition and Transmission Electron Microscopic Characterization of Sub-10-nm Freestanding Pt Nanowires. *Appl. Phys. Lett.* **2006**, *88*, 213116.
(51) Utke, I.; Luisier, A.; Hoffmann, P.; Laub, D.; Buffat, P. A. Focused-Electron-Beam-Induced Deposition of Freestanding Three-Dimensional Nanostructures of Pure Coalesced Copper Crystals. *Appl. Phys. Lett.* **2002**, *81*, 3245−3247.
(52) Takei, T.; Akita, T.; Nakamura, I.; Fujitani, T.; Okumura, M.; Okazaki, K.; Huang, J.; Ishida, T.; Haruta, M. Heterogeneous Catalysis by Gold. In *Advances in Catalysis*; Gates, B. C., Jentoft, F. C., Eds.; Academic Press: New York, 2012; pp 1−126.
(53) Kunz, R. R.; Mayer, T. M. Catalytic Growth Rate Enhancement of Electron Beam Deposited Iron Films. *Appl. Phys. Lett.* **1987**, *50*, 962−964.
(54) Kunz, R. R.; Mayer, T. M. Electron Beam Induced Surface Nucleation and Low-Temperature Decomposition of Metal Carbonyls. *J. Vac. Sci. Technol. B* **1988**, *6*, 1557−1564.
(55) Sachser, R.; Porrati, F.; Huth, M. Hard Energy Gap and Current-Path Switching in Ordered Two-Dimensional Nanodot Arrays Prepared by Focused Electron-Beam-Induced Deposition. *Phys. Rev. B* **2009**, *80*, 195416.
(56) van Dorp, W. F.; Lazić, I.; Beyer, A.; Gölzhäuser, A.; Wagner, J. B.; Hansen, T. W.; Hagen, C. W. Ultrahigh Resolution Focused

DOI: 10.1021/am507327y
ACS Appl. Mater. Interfaces 2015, 7, 2467−2479

Electron Beam Induced Processing: The Effect of Substrate Thickness. *Nanotechnology* **2011**, *22*, 115303.
(57) Botman, A.; Mulders, J. J. L.; Hagen, C. W. Creating Pure Nanostructures from Electron-Beam-Induced Deposition Using Purification Techniques: A Technology Perspective. *Nanotechnology* **2009**, *20*, 372001.
(58) Plank, H.; Noh, J. H.; Fowlkes, J. D.; Lester, K.; Lewis, B. B.; Rack, P. D. Electron-Beam-Assisted Oxygen Purification at Low Temperatures for Electron-Beam-Induced Pt Deposits: Towards Pure and High-Fidelity Nanostructures. *ACS Appl. Mater. Interfaces* **2013**, *6*, 1018−1024.
(59) Stanford, M. G.; Lewis, B. B.; Noh, J. H.; Fowlkes, J. D.; Roberts, N. A.; Plank, H.; Rack, P. D. Purification of Nanoscale Electron-Beam-Induced Platinum Deposits via a Pulsed Laser-Induced Oxidation Reaction. *ACS Appl. Mater. Interfaces* **2014**, *6*, 21256−21263.
(60) Gazzadi, G. C.; Mulders, H.; Trompenaars, P.; Ghirri, A.; Affronte, M.; Grillo, V.; Frabboni, S. Focused Electron Beam Deposition of Nanowires from Cobalt TricarbonylNitrosyl ($Co(CO)_3NO$) Precursor. *J. Phys. Chem. C* **2011**, *115*, 19606−19611.
(61) Miyazoe, H.; Utke, I.; Kikuchi, H.; Kiriu, S.; Friedli, V.; Michler, J.; Terashima, K. Improving the Metallic Content of Focused Electron Beam-Induced Deposits by a Scanning Electron Microscope Integrated Hydrogen−Argon Microplasma Generator. *J. Vac. Sci. Technol. B* **2010**, *28*, 744−750.
(62) Arnold, G.; Timilsina, R.; Fowlkes, J.; Orthacker, A.; Kothleitner, G.; Rack, P. D.; Plank, H. Fundamental Resolution Limits during Electron-Induced Direct-Write Synthesis. *ACS Appl. Mater. Interfaces* **2014**, *6*, 7380−7387.
(63) Friedli, V.; Utke, I. Optimized Molecule Supply from Nozzle-Based Gas Injection Systems for Focused Electron- and Ion-Beam Induced Deposition and Etching: Simulation and Experiment. *J. Phys. D: Appl. Phys.* **2009**, *42*, 125305.

DOI: 10.1021/am507327y
ACS Appl. Mater. Interfaces 2015, 7, 2467−2479